Chapter 7
Superatomic Nanoclusters Comprising Silicon or Aluminum Cages

Atsushi Nakajima

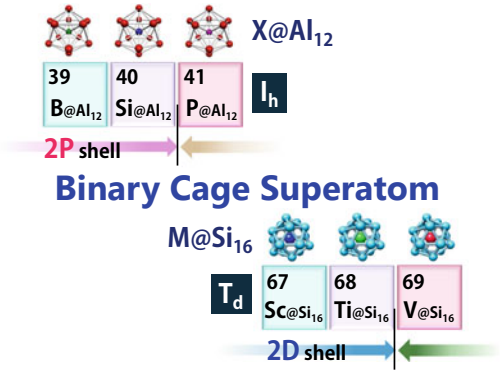

Periodic table for binary cage superatoms of $X@Al_{12}$ and $M@Si_{16}$

T. Ebata and M. Fujii (eds.), *Physical Chemistry of Cold Gas-Phase Functional Molecules and Clusters*,
https://doi.org/10.1007/978-981-13-9371-6_7

Abstract This chapter describes two superatoms, each comprising a central atom and a silicon or aluminum cage. Binary nanoclusters (NCs) at optimized mixing ratios are key components in designing the functionalities relevant to their electronic properties. To form chemically robust functional NCs, it is important to design the cooperatively synergistic effects between the electronic and geometric structures because these stabilize the individual NCs not only against charge transfer into the corresponding cations or anions but also against structural perturbations in their assemblies. Among binary NCs, synergistic effects are particularly expected when one central atom encapsulating cage structure completes a specific electron shell because electronic and geometric factors can operate simultaneously. Although the term "superatom" is widely used when the valence electrons in NCs complete an electron shell, more synergistic effects appear when the superatom adopts a close-packed structure, such as a highly symmetric cage as a binary cage superatom. Representative examples are given for one central atom encapsulated by silicon and aluminum cages, $M@Si_{16}$ and $X@Al_{12}$, their formation and characterization are described, and a large-scale synthetic approach is established for $M@Si_{16}$. The perspectives for binary cage superatom assembly are discussed in terms of theoretical calculations.

Keywords Nanocluster · Superatom · Binary cage superatom · Silicon cage · Aluminum cage, superatom salt · Dimeric superatom · Superatom assembly

7.1 Introduction

Aluminum (Al) and silicon (Si) are elements adjacent to each other in the periodic table. However, their electrical characteristics are distinctly different; Al is highly conductive, while Si is semiconductive. Both are found abundant on the earth, and they are indispensable elements for technological civilizations in modern society.

Si element has greatly contributed to modern society as an excellent semiconductor electronic material from the mid-twentieth century, in terms of innovative progress in informationalization. Particularly, photolithographic cycles for patterning circuits on Si substrates have allowed the development of highly integrated electronic devices by large-scale integration (LSI). Moreover, LSI has been continuously downsized with shorter wavelength lithography until the twenty-first century according to Moore's law [1]. Even though the miniaturization is finally approaching a physical limit of a scale of several nanometers, Si element still plays a central role as the main electronic material in modern society. In contrast to the top-down approach such as

A. Nakajima (✉)
Department of Chemistry, Faculty of Science and Technology, Keio University, 3-14-1 Hiyoshi, Kohoku-Ku, 223-8522 Yokohama, Japan
e-mail: nakajima@chem.keio.ac.jp

Keio Institute of Pure and Applied Sciences (KiPAS), Keio University, 3-14-1 Hiyoshi, Kohoku-Ku, 223-8522 Yokohama, Japan

fine photolithography toward bulk Si, it is also crucial to explore electronic materials by a bottom-up approach using Si atoms.

Beyond the physical limit of several nanometers, creating nanoscale Si compounds can provide novel functionalities, including luminescence and thermoelectric properties [2–5]. Above all, nanoclusters (NCs) of several to hundreds of atomic aggregates allow us to develop the potential for promising Si compounds for exploring the bottom-up Si nanotechnology. When fullerene C_{60} was discovered in a NC beam from carbon vapor [6], much attention was also focused on creating nanoscale Si species having the same cage structure as elemental Si [7, 8], because they belong to the same group in the periodic table. Although further development was required to establish caged Si NCs compared to the progress with C_{60}, recently these showed rich chemistry between the gas phase and the condensed phase [9–13].

A study on the cage structure of Si atoms was reported in 1987 [7]. Based on the mass spectrum, Dr. Beck reported that when one molybdenum (Mo) atom was mixed with Si vapor, $MoSi_{15}^+$ and $MoSi_{16}^+$ cations were generated. He deduced that a Mo atom was contained in a Si cage, which was inferred from analogous metallofullerenes in which metal atoms are contained inside the hollow cage of a carbon fullerene [14]. Although experimental and theoretical studies were extensively performed [15–25], it was not easy to distinguish new nanoscale Si compounds, including a Si cage.

On the other hand, Al element is a low-density metal that is resistant to corrosion, so it is widely used as a building material in the aerospace industry. Al element forms alloys with various elements, widening the diversity of physical properties in various materials. When miniaturizing Al to form NCs, an emerging feature is an electron shell structure [26–28], which was found in NCs consisting of alkali or coinage metals. Particularly, Al_{13}^- affords a 40 electron-completing 2P shell together with an icosahedral close-packed structure, and this is known as a "superatom", mimicking the atomic configuration in the periodic table [29–33]. The novel electronic properties of Al superatoms are intriguing with respect to fabricating nanostructured functional materials.

This chapter describes two binary cage superatoms (BCSs) of metal-atom-encapsulating Si ($M@Si_{16}$) [9–13] and heteroatom-encapsulating Al ($X@Al_{12}$) [34–40] (Fig. 7.1); M = group 3–5 transition metals and X = boron (B), Si, phosphorus (P), scandium (Sc), and titanium (Ti). To form chemically robust functional NCs, it is important to design the cooperatively synergistic effects between electronic and geometric structures because these stabilize the NCs individually not only against charge transfer into the corresponding cations or anions but also against structural perturbations in their assemblies. The synergistic effect is particularly expected for BCSs in which one central atom encapsulating cage structure completes a specific electron counting because electronic and geometric factors can then work simultaneously, retaining their structural symmetry. Although the term "superatom" is widely used when the valence electrons in NCs complete an electron shell [29–33], more synergistic effects appear when the superatom takes a close-packed structure such as a highly symmetric cage as a BCS [13, 38, 39]. For representative examples of $M@Si_{16}$ and $X@Al_{12}$, which have T_d and I_h symmetries, respectively, the formation

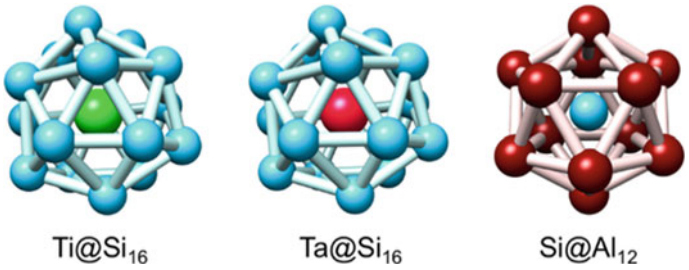

Fig. 7.1 Binary cage superatoms (BCSs) of $M@Si_{16}$ (M = Ti and Ta) and $Si@Al_{12}$. Reprinted with permission from Ref. [13]. Copyright 2017 American Chemical Society

and characterization are described and a large-scale synthetic approach is established for $M@Si_{16}$ [12, 13]. The perspectives for the binary cage superatom assembly are discussed in terms of theoretical calculations [39, 41–43].

7.2 Experimental Methods for Gas Phase Nanoclusters

7.2.1 Dual-Laser Vaporization Nanocluster Source

Figure 7.2 shows a schematic of the NC source of face-to-face laser plasma mixed with pulsed helium (He) carrier gas [44, 45]. An Even-Lavie pulsed valve with a high stagnation pressure of 60–100 atm. [46] was used at a repetition rate of 10 Hz, which was suitable for the effective formation of $MSi_n^{+/0/-}$ and $XAl_n^{+/0/-}$. Intense supersonic He gas pulses were operated to recombine and cool the laser-ablated metal vapor.

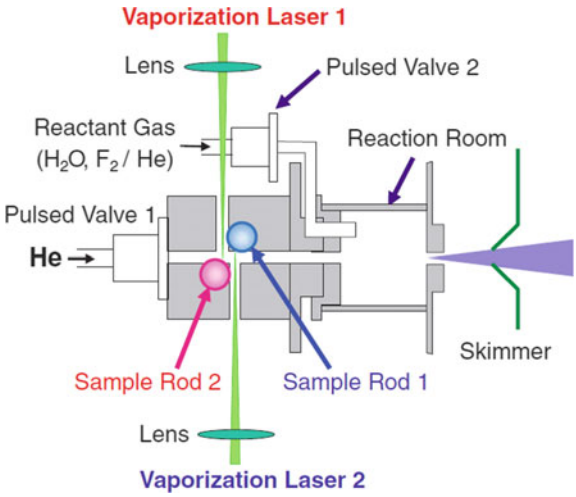

Fig. 7.2 Schematic of a dual-laser vaporization NC source with two sample rods, two pulsed valves, and a reaction room. Reproduced from Ref. [45] with permission from The Chemical Society of Japan

The optimum laser fluence required to maximize the NC intensities depends on the properties of the target under investigation; specifically, the dual-laser vaporization method allows control of the elemental mixing ratio.

The NC source was modified to be "face-to-face" so that the NCs could be more effectively generated [44]. In the primary NC source, two target rods were laterally separated by 4–5 mm, and two lasers independently vaporized their front surfaces. The two lasers then irradiated the two rods with a delay of about 5 μs in synchronization with the speed of the He carrier gas. Hence, in addition to binary mixed NCs, individual NCs consisting of each single element were generated, because the time lag between the vaporization and cooling processes significantly reduces the formation efficiency of the binary NCs.

The focusing positions of the two vaporization lasers were then shifted toward each other by 1.5–2 mm and moved off the front surfaces of the target rods. The shift in the focusing positions facilitated vaporization of the curved surface of the sample rods in a face-to-face manner [47]. The effective mixing of the hot sample plasmas allowed efficient formation of the binary NCs when the two rods were almost simultaneously vaporized, within a few hundred nanoseconds (ns). The simultaneous vaporization enabled us to form binary NCs with one pulsed laser to vaporize the two independent rods, although optimization of the laser fluences became more complex. The mixed vapor formed binary NCs, and their reactivity was examined by exposing reactant gas in the downstream reaction room [48], as shown in Fig. 7.2. The binary NCs passed through a source exit and expanded into a differentially pumped chamber through a skimmer.

7.2.2 Spectroscopic Methods for Nanoclusters

The electronic and geometric structures of the binary NCs were investigated by mass spectrometry, anion photoelectron spectroscopy (PES), and photoionization spectroscopy (PIS). Mass analysis of the neutral binary NCs ionized with an ArF (193 nm; 6.43 eV) or F_2 (157 nm; 7.90 eV) laser and of the charged binary NCs was performed using time-of-flight (TOF) mass spectrometry. For cationic and anionic NCs, the beam was directly accelerated with a pulsed voltage approximately 2 keV, while neutral photoionization with the ArF/F_2 laser was applied in a static electric field of 2 keV. To achieve the appropriate conditions for one-photon ionization of the NCs with the F_2 laser, the laser power dependence was measured by changing the flow rate of He gas toward the laser path tubing between the laser exit and the CaF_2 window of the chamber. A laser fluence below 1 mJ/cm^2 was used, where the ion intensity was linearly dependent on the laser power. For the PIS measurements of the binary NC neutrals, photoionization efficiency curves were measured with a tunable photoionization laser (5.2–6.4 eV) of an optical parametric oscillator (OPO), and the ionization energy was determined from the threshold energy. The laser fluence (typically around 300 μJ/cm^2) was monitored during the measurements to normalize the ion intensities [49].

For the PES measurements of the binary NC anions, a magnetic-bottle-type TOF electron spectrometer was used [50–52]. After mass selection in their TOF with pulse acceleration at 900 eV, their kinetic energy was considerably reduced with a pulsed electric decelerator before they entered the photodetachment region. The fifth harmonic (213 nm, 5.83 eV) of a pulsed Nd^{3+}:YAG laser was then used to irradiate the mass-selected NC anions to detach photoelectrons. The electrons were guided by a strong, inhomogeneous magnetic field with an Nd–Fe–B-based permanent magnet [53], and subsequently by a weak guiding magnetic field produced with an electric current (2–3 A), and detected with a microchannel plate (MCP). Their kinetic energy was analyzed from their TOF and calibrated using the Au^- ($^2S_{1/2} \leftarrow {}^1S_0$) transition [54, 55]. The photoelectron signal was typically accumulated over 20,000–40,000 laser shots.

7.3 Silicon (Si)-based Binary Cage Superatoms (BCSs)

7.3.1 Mass Spectrometry for Si Cage Compounds

In contrast to C_{60}, stable nanoscale compounds comprising only Si atoms have not yet been discovered, but we found that a Si NC containing one metal atom was strongly distributed in the mass spectrum as a magic number by systematically changing the metal atom (M) [9, 44, 45, 56]. To explore the binary M–Si formation, we used the NC source with dual-laser vaporization (Fig. 7.2) to enhance the mixing of hot atomic Si and M vapor, and the NCs produced were mass-analyzed using the TOF spectrometer. The magic number behavior featured with a specific composition coupled with the charge state [9, 45]. Figure 7.3 shows mass spectra for an M–Si NC beam obtained by mixing metal atom M vapor of Sc, Ti, and vanadium (V) of groups 3–5 with Si atoms in the dual-laser vaporization source in cationic, neutral, and anionic charge states. In some TOF mass spectra, the magic number (black arrow) appeared when one M atom is mixed with 16 Si atoms. In nine spectra in Fig. 7.3a–c, the mass spectra in which the magic number appears move from the lower left to the upper right due to the combination of the metal element and charge state [9, 45].

The origin of the magic number is that the NC affords a total valence electron number of 68, and in the Jellium model for NCs with uniform charge distribution [26–28], the 68 electrons correspond to the number of closed shell electrons, up to the 2D shell. Furthermore, the most distinct magic number behavior appears with tantalum (Ta) atoms and in their cations (Fig. 7.3e); $TaSi_{16}^+$ ions are predominant compared to their neighbors [44, 45, 56]. This appears attributable to the interplay between electronic and geometric structures; the $TaSi_{16}^+$ cations afford the total valence electron number of the closed shell and are also stabilized by the size of the Ta atom being most suitable for the inner diameter of the Si_{16} cage. Similarly, $TiSi_{16}$ neutrals are exclusively produced among neutral forms. Therefore, we structurally

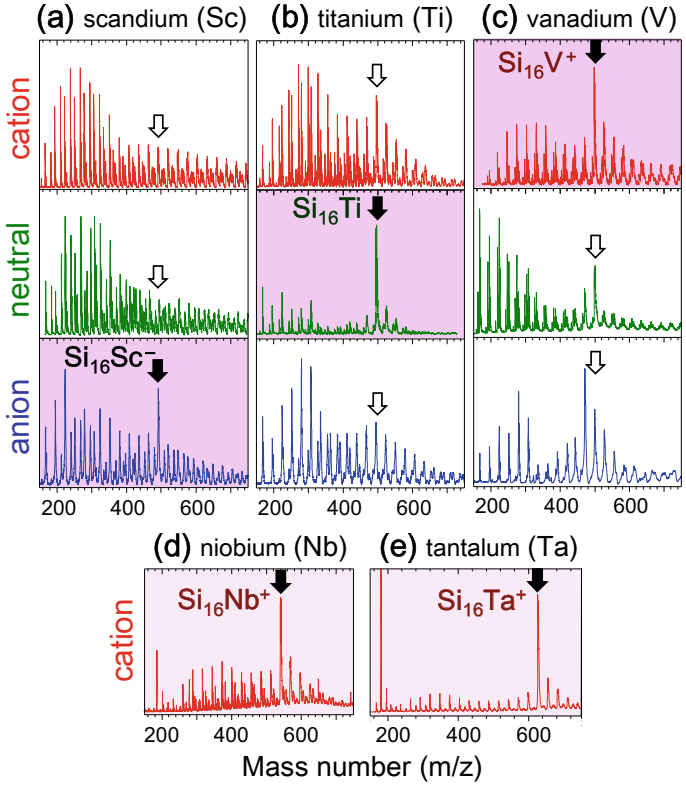

Fig. 7.3 Mass spectra of cations, neutrals, and anions for M–Si NC beam (M = scandium (Sc), titanium (Ti), and vanadium (V)), together with those of niobium (Nb) and tantalum (Ta) cations mixed with Si. Black arrows show magic number peaks, while white arrows show non-magic number peaks. Reproduced from Ref. [45] with permission from The Chemical Society of Japan

evaluated metal-encapsulating Si-based BCSs by further spectroscopic characterization coupled with large-scale synthesis of $Ta@Si_{16}$ and $Ti@Si_{16}$.

To quantitatively evaluate the electronic properties of $M@Si_{16}$, anion PES was used [9]. Figure 7.4 shows the photoelectron spectra for $Sc@Si_{16}^-$, $Ti@Si_{16}^-$, and $V@Si_{16}^-$ using 266 nm (4.66 eV) and 213 nm (5.82 eV) detachment lasers. The binding energies of $Sc@Si_{16}^-$ and $V@Si_{16}^-$ reach 3 eV or more, whereas that of $Ti@Si_{16}^-$ is small at around 2 eV. This shows that the electronic stabilization is large due to the pairing energy when the total number of valence electrons in the anion is an even number, while an odd number makes the anion unstable.

The threshold binding energy corresponds to the *EA* of the corresponding neutral, and the *EA* is shown in Fig. 7.4. Moreover, since $Sc@Si_{16}^-$ possesses 68 electrons to complete the 2D shell, $Ti@Si_{16}^-$ has one excess electron, and thus the peak labeled X in the $Ti@Si_{16}^-$ spectrum appears to be an additional peak to that of $Sc@Si_{16}^-$. To confirm that peak X corresponds to a singly occupied molecular orbital (SOMO),

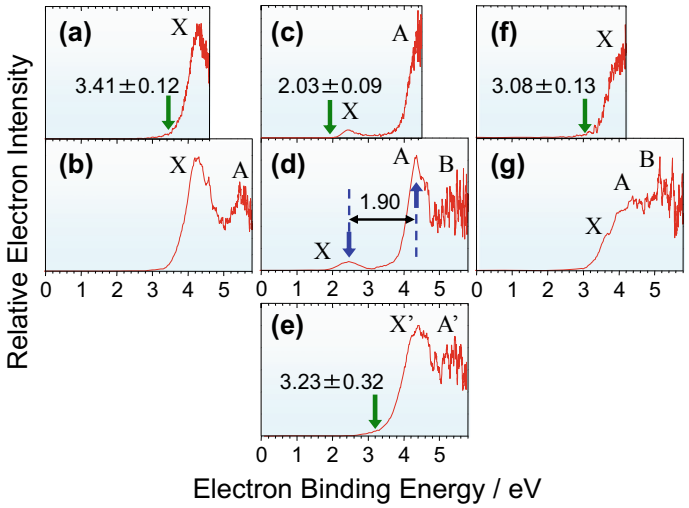

Fig. 7.4 Photoelectron spectra of BCS anions of $Sc@Si_{16}^-$ **a**, **b**, $Ti@Si_{16}^-$ **c**, **d**, and $V@Si_{16}^-$ **f**, **g** at 266 nm (4.66 eV; top three spectra) and at 213 nm (5.82 eV; bottom four spectra). Comparing the photoelectron spectrum of $Ti@Si_{16}^-$ with that of $Ti@Si_{16}F^-$ **e** enables us to assign the HOMO–LUMO gap. Reprinted with permission from Ref. [9]. Copyright 2005 American Chemical Society

$Ti@Si_{16}F^-$ was generated by adding an F atom to $Ti@Si_{16}^-$ and the photoelectron spectrum was obtained [57–59]. As shown in Fig. 7.4e, peak X disappears for $Ti@Si_{16}F^-$ while the spectral features in the higher binding energy region are retained.

This is because the F atom (with one electron deficient) effectively accommodates one electron into a deeper MO. The spectral change enables us to assign peak X as the SOMO and to evaluate the gap between the highest occupied MO (HOMO) and the lowest unoccupied MO (LUMO) to be 1.90 eV, as shown in Fig. 7.4d. The HOMO–LUMO gap is considerably larger than that of C_{60} (1.57 eV) [60], demonstrating the high stability of the $Ti@Si_{16}$ BCS. As suggested by theoretical calculations [61], cage "aromaticity" might be an important determinant of the electronic stability of the BCSs.

7.3.2 Development of Intense Nanocluster Source with Magnetron Sputtering

The dual-laser vaporization source is very powerful to allow investigation of binary NC formation by changing the combinations of two different elements. However, structural analysis methods, such as nuclear magnetic resonance (NMR) and Raman spectroscopy, often require enhancement of the total number of NCs. Furthermore,

for well-controlled soft-landing, it is necessary to reduce the kinetic energy distribution of the beam, because a wide energy distribution might cause dissociation of the NCs in collisions with the substrate to which a bias voltage is applied [62]. Based on the production amount and narrow kinetic energy distribution, compared to laser evaporation, it is advantageous to use a magnetron sputtering method in which larger targets are available and NCs are formed in a steady flow of inert cooling gas, as shown in Fig. 1.14 [63, 64]. To form binary NCs, two choices are available: dual magnetron sputtering with two targets or single magnetron sputtering with a mixed target. Since the targeted BCSs of $M@Si_{16}$ have a specific composition, it is convenient to use a mixed target to produce a stable beam from merging nascent atomic vapor. Considering the sputtering rates of each element, the mixing ratios of the target are optimized for generating $M@Si_{16}$ BCSs.

Particularly, size-selective soft-landing is performed only for charged NCs excluding neutrals, and then the NC ion density should be enhanced to efficiently accumulate the selected NCs on a substrate. For magnetron sputtering, high-power impulse magnetron sputtering (HiPIMS) [65–67] with a pulsed power supply increases the ion density while maintaining the average output. The HiPIMS NC source can provide 2–10 times higher ion density compared to conventional magnetron sputtering using a static DC power supply.

7.3.3 *Immobilization and Characterization of Si-based BCSs on Solid Surface*

Using a quadrupole mass filter, only $Ta@Si_{16}^{+}$ BCS ions formed in the developed NC source were selected, and these were deposited and immobilized on a solid substrate [10, 68]. During the selective deposition, the $Ta@Si_{16}$ produced is deposited under soft-landing conditions (kinetic energy below 1 eV per atom) to avoid destruction when colliding with the substrate. When the deposited $TaSi_{16}$ was characterized by X-ray photoelectron spectroscopy (XPS) (Fig. 7.5) [11, 69, 70], both Si 2*p* and Ta 4*f* exhibit sharp peaks, showing (1) the preserved 1:16 composition of Ta:Si based on their intensity ratio and (2) a single chemical environment for each element based on their peak envelopes. These results can be explained by the Ta atom being encapsulated by the Si_{16} cage, because other structures, such as linear, two-dimensional planar ones would have provided broader XPS peaks due to different chemical environments for Si and Ta atoms. When the deposited substrate is heated to 350°C, although $TaSi_{16}$ reacts slightly with residual oxygen, its oxidation initially occurs at Si atoms (Fig. 7.5, bottom), while Ta is not oxidized [11]. Generally, since naked Ta is more easily oxidized than Si [71, 72], the Ta atom must be encapsulated inside the Si_{16} cage (hereafter referred to as $Ta@Si_{16}$). In this soft-landing method, $Ta@Si_{16}$ can be deposited on the substrate to form several layers, but it is highly desirable to construct a more efficient synthesis methodology for further nanomaterial science as well as developing detailed structural analyses.

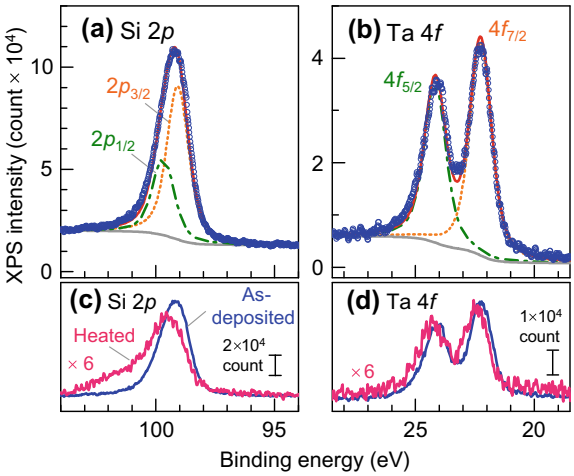

Fig. 7.5 XPS spectra of Ta@Si_{16} BCS deposited on HOPG around **a** Si 2*p* and **b** Ta 4*f* core levels. The fitted results (red line) and spin-orbit contributions (orange dotted line and green dash-dotted line) are superimposed in (**a**) and (**b**). Background-subtracted XPS spectra of the Ta@Si_{16} BCS film for **(c)** Si 2*p* and **(d)** Ta 4*f* before and after heating (720 K, 16 h) are shown by blue and red lines, respectively. Reprinted with permission from Ref. [11]. Copyright 2015 American Chemical Society

7.3.4 Dispersion Trapping of Si-Based BCSs in Liquid

To identify the structure of the metal-atom-encapsulating Si_{16} cage, a new apparatus was designed and constructed, as shown in Fig. 7.6, in which species generated in the beam with HiPIMS are dispersed in liquids by a direct liquid embedded trapping (DiLET) [12, 13]. The DiLET is based on the idea that chemical isolation toward liquids trapping all beam species is much more efficient than the size-selective deposition, because (1) neutral NCs can also be captured by liquids and (2) the ion transmittance in the mass selection is as low as 20%. Since the NC source operates under vacuum, a liquid with a low vapor pressure must be used to achieve a vacuum of around 10^{-2} Pa, and thus NCs are injected into polyethylene glycol dimethyl ether (PEG-DME) liquid. During injection, a fresh liquid surface must be prepared to prevent aggregation of various NCs, and then the liquid is stirred vigorously during beam injection. Liquid trapping was applied to Ti@Si_{16} as well as Ta@Si_{16} using a Ti or Ta mixed Si disk target. As the beam was injected into the PEG-DME liquid, the transparent liquid became brown after about 1 h, and after about 3 h, the liquid was removed from the chamber and treated in a glove box under reduced oxygen and moisture. While purifying and isolating the liquid with appropriate solvents, fractionation was repeated three times by changing the mixing ratio of nonpolar hexane and large polar tetrahydrofuran (THF), and finally a fraction soluble in pure THF was obtained.

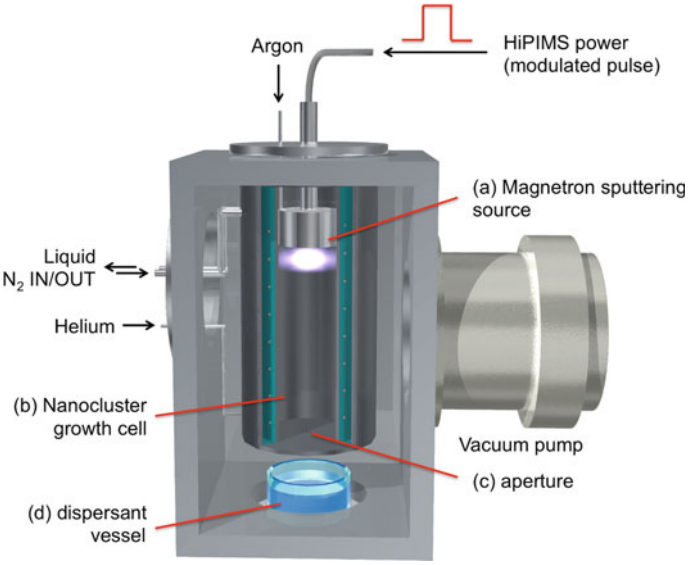

Fig. 7.6 Schematic of NC synthesis apparatus based on HiPIMS and DiLET. Reprinted with permission from Ref. [12]. Copyright 2017 American Chemical Society

7.3.5 Structural Analysis of Si-based BCSs

The resulting fraction was analyzed by XPS, ^{29}Si-NMR, Raman spectroscopy, and quantum chemistry calculations [12]. First, XPS was performed for the obtained Ta–Si fraction, and the Si 2*p* and Ta 4*f* spectra were consistent with those in Fig. 7.5. This clearly demonstrates that Ta@Si_{16} BCSs in the beam can be successfully dispersed in PEG-DME liquid and that Ta@Si_{16} BCSs can be obtained as stable species even after both solvent extraction and ligation with PEG-DME. In fact, the isolation of Ta@Si_{16} BCSs was also confirmed by mass spectrometry [12]. Furthermore, in the Raman spectra, broad peaks were observed at around 120, 300, and 450 cm^{-1} for both Ti–Si and Ta–Si (upper traces in Fig. 7.7a, b). Importantly, the features of these Raman spectra are consistent with those of naked BCSs in the surface-enhanced Raman spectra (SERS) (lower traces in Fig. 7.7a, b), which are obtained by depositing exclusively Ti@Si_{16} or Ta@Si_{16} BCS ions on the substrate.

Furthermore, the successful synthesis of M@Si_{16} BCSs on a 100 mg scale enables us to apply NMR measurements; ^{29}Si–NMR spectra for Ti@Si_{16} and Ta@Si_{16} exhibit one and two peaks, respectively, between 100 and −100 ppm (Fig. 7.8). Although these peak positions are inconsistent with the predictions obtained from quantum chemistry calculations, the result suggests (1) the difficulty of calculation-based prediction, (2) the weak coordination effect of PEG-DME, and (3) structural fluctuations of the Si_{16} cage. Based on these spectroscopic structural evaluations, it was concluded that both Ti@Si_{16} and Ta@Si_{16} BCSs are identified as tetrahedral structures of Si_{16}

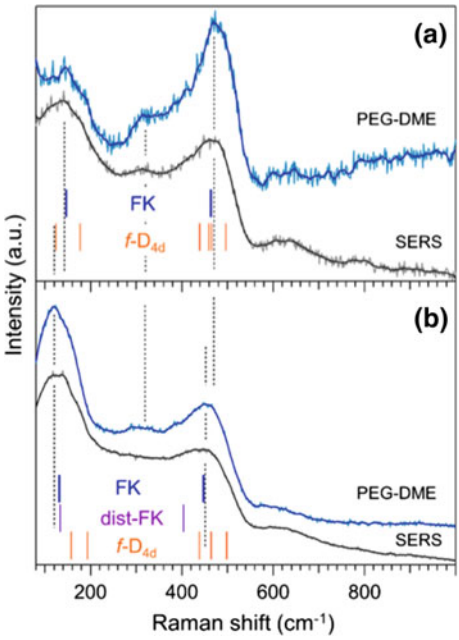

Fig. 7.7 Raman spectra excited at 532 nm for isolated M@Si_{16}:PEG-DME BCS and size-selected naked M@Si_{16} BCS on the SERS substrate (M@Si_{16}/Ag/$SrTiO_3$); M = (**a**) Ti and (**b**) Ta. Stick bars represent the selected Raman active modes calculated by DFT for FK, dist-FK, and *f*-D_{4d} isomers. Reprinted with permission from Ref. [12]. Copyright 2017 American Chemical Society

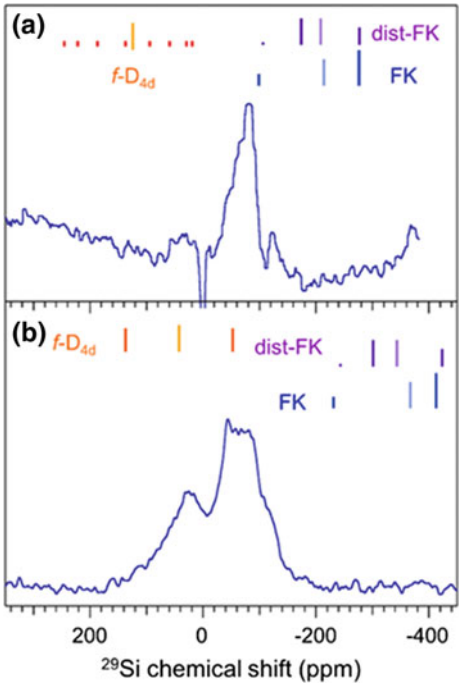

Fig. 7.8 ^{29}Si NMR spectra of M@Si_{16}:PEG-DME BCS dispersed in THF for M = Ti (300 K) and for M = Ta (318 K). Stick bars represent chemical shifts (CSs) calculated by ZORA-DFT for FK, dist-FK, and *f*-D_{4d} isomers at the PBE0/TZ2P level. The CSs averaged over the sites are shown with faint colors. Reprinted with permission from Ref. [12]. Copyright 2017 American Chemical Society

derived from the Frank-Kasper (FK) structure: a metal-encapsulating tetrahedral Si cage (METS) (Fig. 7.1) [12, 13].

7.4 Aluminum (Al)-based Binary Cage Superatoms (BCSs)

7.4.1 Mass Spectrometry of Al-based BCSs

7.4.1.1 Aluminum–Silicon

Figure 7.9 shows the mass spectra of the Al–Si NC anions, neutrals, and cations produced [38, 39]. In the photoionization of the Al_nSi_m neutral, the laser power dependence indicated that one-photon ionization occurred with the F_2 laser (7.90 eV). Since the mass of Si (28 u) is very close to that of Al (27 u), the mixed Al–Si NCs form bundles of mass peaks for each $n + m$. Although the most intense mass peaks were observed at $n + m = 13$ in the mass spectra, high-resolution TOF mass spectrometer [73] revealed that the most abundant peak is systematically changed. The right-hand figures in Fig. 7.9 show intensity distributions at $n + m = 13$, the most abundant 13-mers being Al_{13}^- for anions, $Al_{12}Si$ for neutrals, and $Al_{11}Si_2^+$ for cations. The

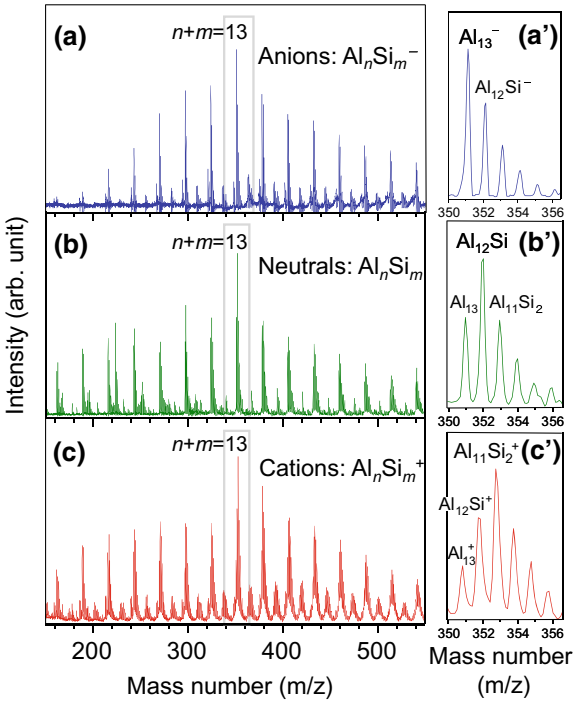

Fig. 7.9 Mass spectra of the Al–Si NC anions, neutrals, and cations. The Al_nSi_m neutrals are photoionized with the F_2 laser (7.90 eV). The most intense mass peaks are observed at $n + m = 13$ in the mass spectra; intensity distributions at $n + m = 13$ are shown in the right-hand figures, The most abundant 13-mers are the Al_{13}^- anion, $Al_{12}Si$ neutral, and $Al_{11}Si_2^+$ cation. Reprinted with permission from Ref. [38]. Copyright 2006 American Chemical Society

charge state dependence for the most abundant Al_{13}^-, $Al_{12}Si$, and $Al_{11}Si_2^+$ shows that the doped Si atoms function as a tetravalent atom to satisfy 2P shell closure(40 e) in the Al to Si substitution, because both $Al_{12}Si$ and $Al_{11}Si_2^+$ NCs possess 40 valence electrons in common in addition to Al_{13}^-. Furthermore, a charge state dependence is observed in the size-dependent abundance in the mass spectra. Figure 7.10 shows the intensity distributions of the Al_n^- and Al_nSi^- anions, Al_nSi neutrals, and Al_nSi^+ and $Al_nSi_2^+$ cations. Some intensity distributions exhibit magic number behavior at $n + m = 13$, representing the above-mentioned Al_{13}^-, $Al_{12}Si$, and $Al_{11}Si_2^+$. These results clearly confirm that the substitution of Si atoms corresponds to one-electron addition toward the total number of valence electrons in the Al–Si binary NCs.

As reported earlier [15, 38], the chemical stability of the Al_nX NCs can be examined using a chemical probe method. When the adsorption reactivity of the Al–Si binary NCs is measured toward O_2 reactant gas, $Al_{12}Si$ neutrals show prominent chemical inertness compared to the others [39], as shown in Fig. 7.11. In fact, $Al_{12}Si$ neutrals are favored electronically as well as geometrically. A plausible explanation is that $Al_{12}Si$ adopts a closed electron configuration when a tetravalent Si atom dopant completes the 2P electron shell combined with the valence electrons of *sp*-hybridized Al atoms [36, 37, 74, 75]. Furthermore, the diameter of a Si atom (1.18 Å) is slightly

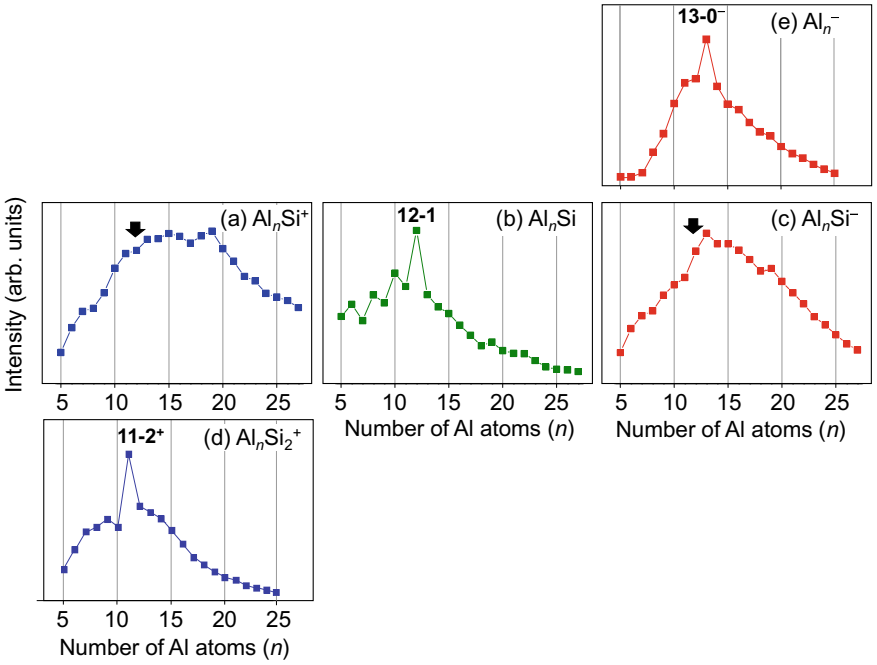

Fig. 7.10 Intensity distributions of the Al_nSi^+ and $Al_nSi_2^+$ cations, Al_nSi neutrals, and Al_n^- and Al_nSi^- anions. A prominent peak appears at $n + m = 13$ for $Al_nSi_2^+$, Al_nSi, and Al_nSi^-. Solid arrows show the positions for $Al_{12}Si^{+/-}$. Reprinted with permission from Ref. [38]. Copyright 2006 American Chemical Society

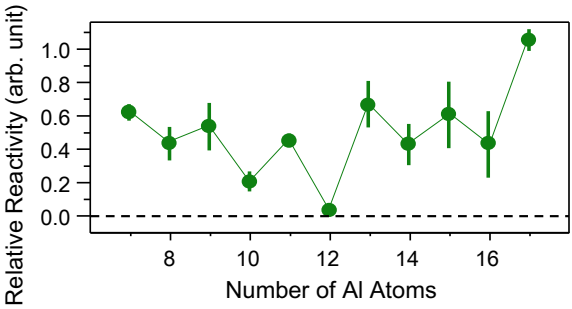

Fig. 7.11 Plots of the relative reactivity of the Al_nSi_1 NCs against exposure to O_2 at $n = 7$–17 with experimental uncertainties. Reproduced from Ref. [39] with permission from the PCCP Owner Societies

smaller than that of an Al atom (1.43 Å) [76], leading to geometric stabilization owing to less distorted icosahedral structures. In order to make the icosahedral Al_{13} more geometrically stable, the Al_{12} cage favors a smaller central atom, because the distance between adjacent surface atoms is distortedly extended by 5% compared to the distance between the central and surface atoms [34, 77].

7.4.1.2 Aluminum–Boron

As described in the previous section, when one Al atom is substituted with a Si atom in the Al_{13}^- superatoms, the Si atom is located at a central atom in the icosahedron, resulting in: (1) relaxation of structural distortions intrinsically relevant to the icosahedral structure and (2) neutralization of the negative Al_{13}^- ion due to one-electron addition with a tetravalent Si atom, forming $Si@Al_{12}$ BCS. Similar structural relaxation is expected for boron (B), because B is a smaller atom than Al, with both belonging to group 13.

Figure 7.12 shows a mass spectrum of Al NC anions mixed with B atoms [34]. As seen in the distributions for the number of boron atoms (Fig. 7.13; $m = 0, 1, 2,$

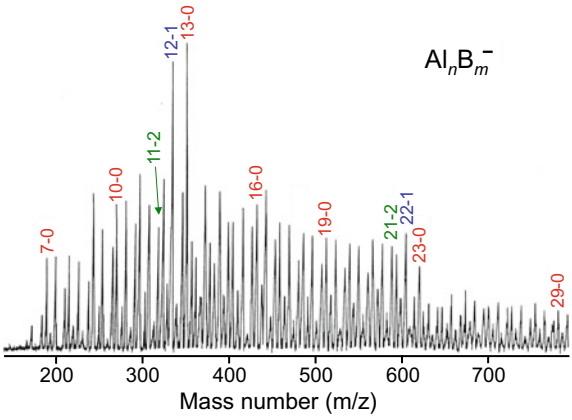

Fig. 7.12 Mass spectrum of the Al–B nanocluster anions ($Al_nB_m^-$). The most intense mass peaks are observed at $n + m = 13$–0 and 12–1 along with some enhancements around $n + m = 23$. Reprinted from Ref. [34] with permission from Elsevier

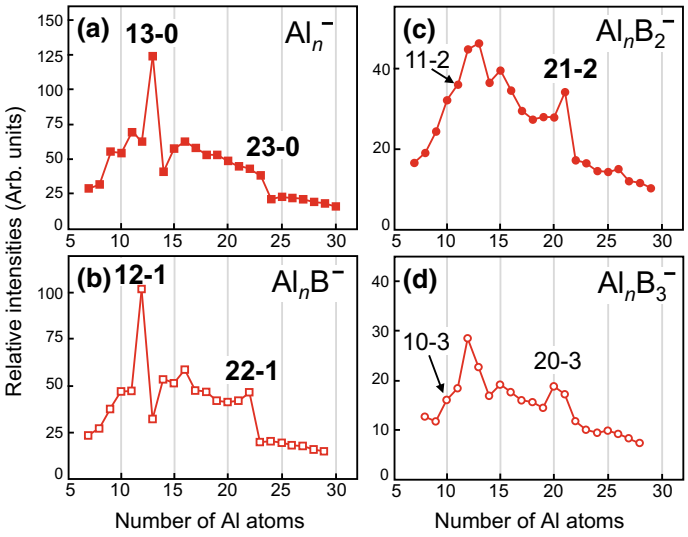

Fig. 7.13 Intensity distributions of the $Al_nB_m^-$ anions **a** $m = 0$, **b** $m = 1$, **c** $m = 2$, and **d** $m = 3$). Magic number behavior appears at $n + m = 13$ and 23, while it disappears at $n - m = 11$–2 and 10–3. Reprinted from Ref. [34] with permission from Elsevier

and 3), a distribution maximum is observed at $n - m = 13$–0 and similarly at 12–1, where an Al atom is substituted with a B atom. However, when two B atoms are substituted, no local maximum is observed at 11–2, showing that the second B atom destabilizes 12–1. The results suggest that at 12–1 the B atom is encapsulated in an Al_{12} cage, and that the second B atom destabilizes the icosahedral cage from Al_{12} to $Al_{11}B$ due to a vertex-replaced icosahedron (exohedral B@$Al_{11}B$) with a smaller surface B atom.

In the distributions shown in Fig. 7.13a, larger Al NC anions also exhibit magic number behavior, particularly at $n = 23$, although this is less prominent compared to $n = 13$. Al_{23}^- electronically satisfies the 3S shell closure by 70 electrons [34]. The behavior of the Al–B distributions in Fig. 7.13b–d suggests that the local maximum at $n + m = 23$ is retained with substitution of up to two B atoms but the third B atom ($m = 3$) makes the Al_{23} derivatives less stable. This suggests that the two B atoms are encapsulated in the Al cage, while the third B atom becomes a surface atom. The structure of $Al_{21}B_2$ is discussed below together with that of $Al_{21}Si_2$.

7.4.2 Anion Photoelectron Spectroscopy for Al-based BCSs

To quantitatively evaluate the electronic properties, anion PES was used for these two binary NCs. Figure 7.14 shows photoelectron spectra of $Al_{12}Si^-$, $Al_{12}SiF^-$, $Al_{12}B^-$, and $Al_{13}Cs^-$ [37, 38, 75]. In the $Al_{12}Si^-$ spectrum, a small peak (label X) is observed

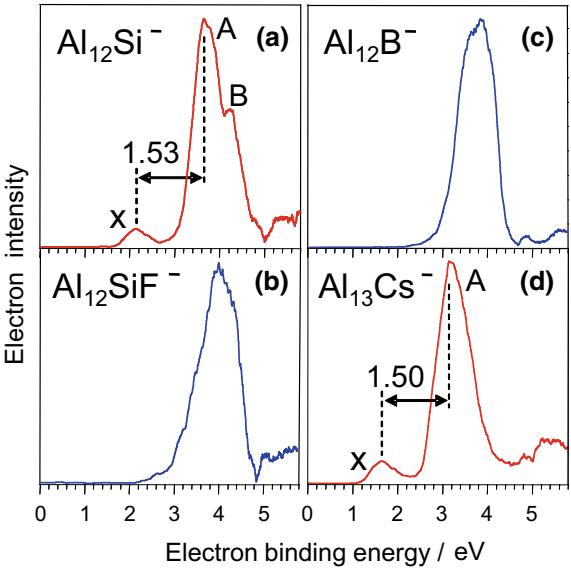

Fig. 7.14 Photoelectron spectra of **a** $Al_{12}Si^-$, **b** $Al_{12}SiF^-$, **c** $Al_{12}B^-$, and **d** $Al_{13}Cs^-$ at 213 nm (5.82 eV). Reprinted with permission from Ref. [38]. Copyright 2006 American Chemical Society

at 1.5 eV following a large peak at around 3.5 eV, and the *EA* is as small as about 1.5 eV. The spectral feature is attributed to one-electron addition to the 40 electron closed shell of neutral $Al_{12}Si$, resulting in the excess electron occupying the orbital above the HOMO of $Al_{12}Si$. In fact, the F-atom adduct of $Al_{12}SiF^-$ anion can be selectively produced when Al–Si NC anions are reacted with fluorine (F_2) gas [38, 39], which is seemingly promoted by the excess electron in $Al_{12}Si^-$.

When the photoelectron spectrum of the $Al_{12}SiF^-$ product is obtained, the peak X observed in Fig. 7.14a disappears while maintaining the other features, as shown in Fig. 7.14b. Furthermore, the spectrum of $Al_{12}SiF^-$ is almost the same as those of Al_{13}^- and $Al_{12}B^-$ (Fig. 7.14**c**). Namely, by adding the F atom [57–59], the excess 41st electron is scavenged into a deeper level by the F atom, forming a combination of $Al_{12}Si$ neutral and F^-, as discussed for $Ti@Si_{16}^-$ and $Ti@Si_{16}F^-$ in Sec. 7.3.1. The results show that the peak X of $Al_{12}Si^-$ is attributable to a SOMO, with a gap of 1.53 eV between the HOMO and the LUMO for $Al_{12}Si$ from the two peak intervals.

Furthermore, the NC anions of both Al_{13}^- and $Al_{12}B^-$ satisfy 40 electron shell closure, and they become 41st electron systems when a cesium alkali metal atom (Cs) is added [35, 36, 38, 78]. Interestingly, as shown in Fig. 7.14d, the peak X appears in a low binding energy region, and the photoelectron spectrum is almost the same as that of $Al_{12}Si^-$. Specifically, the $Al_{13}Cs$ neutral is a 40 electron species, forming a superatomic salt of $(Al_{13}^-)(Cs^+)$ between the halogen-like Al_{13} superatom and the alkali metal atom [35, 38].

7.4.3 Photoionization Spectroscopy for Al-based BCSs

The E_i of the neutral NCs can be evaluated by measuring the photoionization efficiency curve with a tunable photoionization laser [38, 39, 49]. Figure 7.15 shows the size-dependent E_i values of Al_n, Al_nSi, and Al_nSi_2 [39], and these asymptotically approach 4.08 eV of the Al metal work function [76] as the size increases. Along with the asymptotic E_i decrease, a discontinuous change in E_i is found when crossing the closed shell of a specific electron shell, the 40 electron boundary.

The E_i values of the Al_{13} and $Al_{12}Si$ neutrals reach 6.42 eV or more. When one Al atom is added to these to form Al_{14} and $Al_{13}Si$, their E_i values drop drastically to around 5.6 eV. A similar E_i drop is observed when one Al atom in $Al_{12}Si$ is substituted with a Si atom to form $Al_{11}Si_2$. These discontinuous drops in E_i values can be explained in terms of electron occupation above the 40 electron shell closure. A local maximum/minimum in E_i attributable to a similar electron shell is also observed around 70 electrons (3S shell), the local E_i maximum for $Al_{22}Si$ and the local E_i minimum for $Al_{21}Si_2$, which are treated as a closed shell of 70 electrons and a one-electron excess of 71 electrons, respectively.

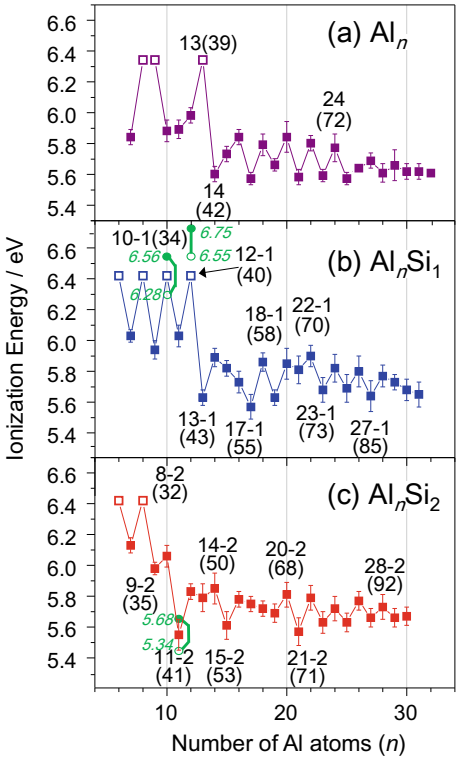

Fig. 7.15 Ionization energies of neutral Al_nSi_m NCs in eV; **a** $m = 0$, **b** $m = 1$, and **c** $m = 2$. The open squares around 6.4 eV show that E_i value is between 6.42 and 7.90 eV, where they can be ionized not by ArF laser (193 nm; 6.42 eV) but by F_2 laser (157 nm; 7.90 eV). Calculated ionization energies for some NCs are shown along with their values, where open and solid circles show adiabatic and vertical ionization energies, respectively. The compositions of local maxima and minima are shown with the total valence electrons in parentheses. Reproduced from Ref. [39] with permission from the PCCP Owner Societies

For another Al-based binary NC doped with phosphorus (P) atoms, the substitution of an Al atom with P adds two valence electrons because of the pentavalent P atom [38]. The E_i of $P@Al_{12}$ is as low as 5.37 eV, showing a one-electron excess against the 40 electron shell closure, and the E_i is the lowest value compared with those of similarly sized NCs. This feature is consistent with the total valence electron number of $P@Al_{12}$ of 41, causing $P@Al_{12}$ to act as an alkali metal-like BCS.

7.4.4 Theoretical Calculations for Al-Based BCSs

These quantitative experimental evaluations allow us to clarify the electronic and geometric properties of $Al_{12}X$ and $Al_{21}X_2$ NCs in detail using quantum chemistry calculations [39, 40, 42, 43]. Figure 7.16 shows optimized structures of cations, neutrals, and anions of $Al_{12}Si$, where two isomeric forms are shown; endohedral Si in an icosahedral Al_{12} cage and a vertex-replaced icosahedron (exohedral Si atom) [39]. In any charge state, $Si@Al_{12}$ with a central Si atom is calculated to be more stable than the vertex-replaced one.

When one electron is depleted or in excess to form $Al_{12}Si^+$ or $Al_{12}Si^-$, the encapsulated Al_{12} cage structure is unchanged, but the structural symmetry is lowered from I_h symmetry. The lowering of symmetry is caused by the Jahn–Teller effect, in which the NCs are electronically stabilized by structural distortion associated with the undegeneration of electronic states [76]. Retaining the cage structure against charge exchange among $Al_{12}Si^{+/0/-}$ implies that the $Si@Al_{12}$ superatoms are stable against charge transfer, indicating that these are promising BCSs for fabricating BSC assemblies for an electronic device.

Additionally, molecular orbital (MO) diagrams are obtained from the optimized Al_{13}^-, $Al_{12}Si^-$, and $Al_{12}SiF^-$, as shown in Fig. 7.17 [38, 39]. In Al_{13}^- and $Al_{12}SiF^-$, the HOMO–LUMO gap is large, which is consistent with the experimental results shown in Fig. 7.14. Furthermore, in $Al_{12}Si^-$, the SOMO level appears below the LUMO level, represented by a small bump in the photoelectron spectrum in Fig. 7.14.

$X@Al_{12}$ (X = B, Si, and P) BCSs behave as halogen-like, rare gas-like, and alkali metal-like superatoms, respectively [38, 39, 79–81], where smaller atoms, from trivalent to pentavalent atoms of main group elements, are preferred as the central atom. To verify whether electron shell closure occurs by doping transition metals, the electronic properties were examined for $Al_{12}M$ doped with trivalent Sc and tetravalent Ti [40]. It was found that neither Sc nor Ti atoms were encapsulated in the Al_{12} cage due to their large atomic radius; instead, they formed a vertex-replaced structure, exohedral $Al_{12}M$. In addition, their electronic states are described not by 40 electron shell closure, but according to the Wade-Mingos rule, in which $Al@Al_{11}$ is bonded to a transition metal atom, as shown in Fig. 7.18.

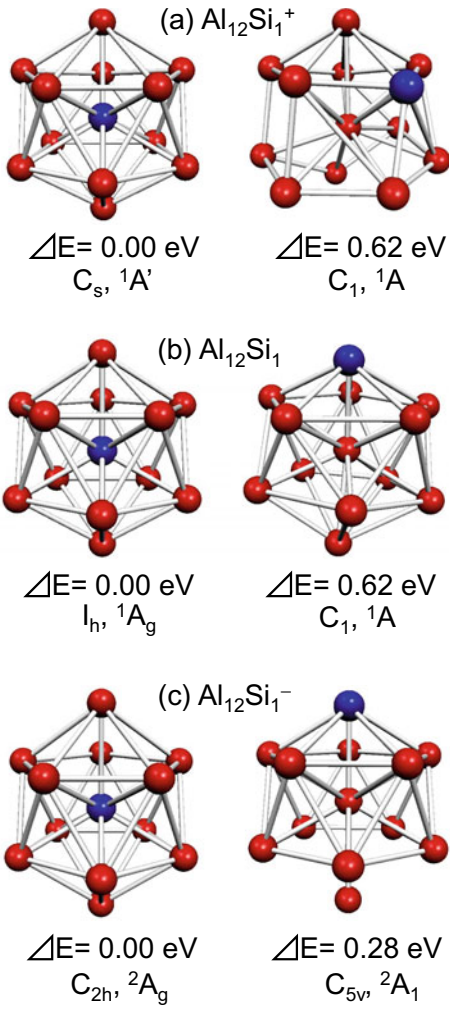

Fig. 7.16 Calculated equilibrium structures and energy differences between isomers with central Si and surface Si; **a** $Al_{12}Si_1^+$, **b** $Al_{12}Si_1$, and **c** $Al_{12}Si_1^-$. Al and Si atoms are shown as red and blue, respectively. Reproduced from Ref. [39] with permission from the PCCP Owner Societies

7.4.5 Size Evolution of Al-Based Nanoclusters for Assembled Materials

In the size dependence of E_i shown in Fig. 7.15, features based on electron shell closure appear not only in the vicinity of Al_{13} but also around Al_{23}; for $Al_{21}Si_2$, the local E_i minimum is due to 3S shell closure (70 e). It appears reasonable that both B and Si atoms tend to be encapsulated in Al NCs as demonstrated for $B@Al_{12}$ and $Si@Al_{12}$. Based on the icosahedral Al_{12} cage, a face-sharing bi-icosahedral structure is conceivable for $Al_{21}B_2$ and $Al_{21}Si_2$ [39, 43], and then the lowest-energy isomer can be calculated.

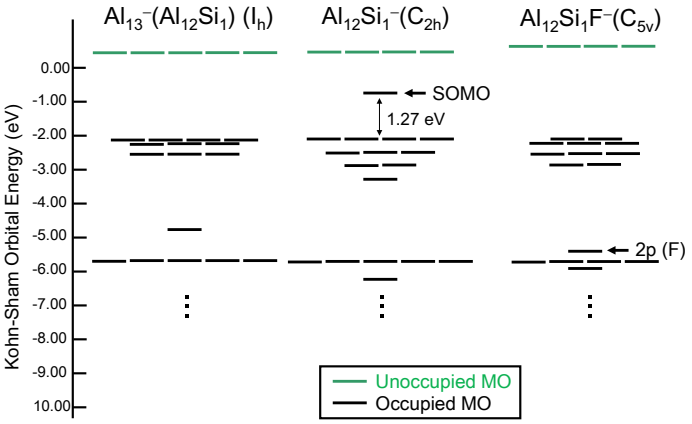

Fig. 7.17 Molecular orbital diagrams of Al_{13}^- ($Si@Al_{12}$), $Si@Al_{12}^-$, and $Si@Al_{12}F^-$. Both Al_{13}^- ($Si@Al_{12}$) and $Si@Al_{12}F^-$ have large HOMO–LUMO gap, whereas $Si@Al_{12}^-$ has SOMO. Reproduced from Ref. [39] with permission from the PCCP Owner Societies

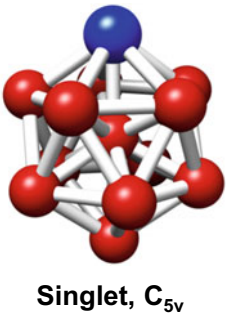

Fig. 7.18 Equilibrium structure of $Al_{12}Sc^-$ NCs calculated at the PBE0/def-SV(P) level (Al; red and Sc; blue). Reproduced from Ref. [40] with permission from IOP Publishing

For $Al_{21}B_2$, optimization from the initial structure of the face-sharing bi-icosahedral structure affords a triangular rice-ball structure containing two B atoms [43]. For $Al_{21}Si_2$, however, it was calculated that a face-sharing bi-icosahedron is more stable than a triangular structure for cations and neutrals [39], as shown in Fig. 7.19. The structure shares an Al trimer on the cage surface, with a partial overlap of the two icosahedral $Si@Al_{12}$.

More interestingly, it was found that the superatomic orbital (SAO) of $Al_{21}Si_2$ can be represented by superposing two $Si@Al_{12}$ superatoms. Figure 7.20 shows the energy diagrams of the $Al_{21}Si_2$ bi-icosahedron, which shares an Al trimer between two $Si@Al_{12}$. Using a linear combination of SAOs (LCSAO) [39], a MO picture for dimeric superatoms (di-SAs) is obtained similar to linear combinations of atomic orbitals (LCAOs); the 2Pσ* LCSAO-MOs for $Al_{21}Si_2^+$ cations and $Al_{21}Si_2$ neutrals are vacant and SOMO, respectively, while up to the 1Fδ* LCSAO-MO the MOs are occupied. For di-SA, the orbital shapes of the SAOs allow wavefunction overlap at closer distances between the two superatoms compared to that between the atomic

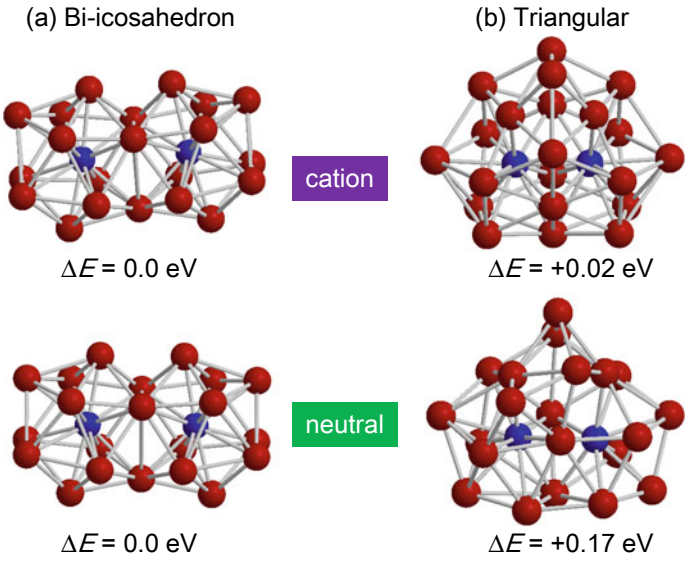

Fig. 7.19 Calculated equilibrium structures and energy differences between two isomers of **a** bi-icosahedron and **b** triangular form for cationic and neutral $Al_{21}Si_2$ with PBE1PBE/6-311+G*. The experimental ionization energy is reproduced by the bi-icosahedrons. Reproduced from Ref. [39] with permission from the PCCP Owner Societies

orbitals of homonuclear diatomics. This feature gives an orbital stability of di-SA in the order of $\sigma < \pi < \delta < \phi$, because the nature of the LCSAO-MOs is closer to the united (super)atom limit than that of the homonuclear diatomics (LCAO-MOs).

Furthermore, the electronic properties of the superatom dimers of $X@Al_{12}$–$Y@Al_{12}$ (X–Y = Si–Si, B–P, Al–P), hetero-assemblies of endohedral Al–based BCSs, are theoretically predicted, where the optimized dimers are obtained by facing the sides of the monomers in a staggered fashion [42]. When the electronic absorption spectra are calculated for the $B@Al_{12}$–$P@Al_{12}$ and Al_{13}–$P@Al_{12}$ heterodimers (a combination between halogen-like and alkali metal-like superatoms), a CT band from $B/Al@Al_{12}$ to $P@Al_{12}$ is found in the visible region. The charge distributions in the heterodimer of $B@Al_{12}$–$P@Al_{12}$ are unchanged by inserting $Si@Al_{12}$ between the two superatoms, and the dipole moment of the heterotrimer (3.89 D) is larger than that of the heterodimer (2.38 D). Similarly, a heterodimer and trimer comprising Si-based BCSs, $M@Si_{16}$ (M = Sc, Ti, and V), are predicted to exhibit electronic excitation involving CT states; this is characterized as electron transfer from $V@Si_{16}$ to $Sc@Si_{16}$ in the heterodimer of $V@Si_{16}$–$Sc@Si_{16}$ with a dipole moment of 7.63 D [41]. When the $Ti@Si_{16}$ BCS is inserted between the $V@Si_{16}$–$Sc@Si_{16}$ dimer, the linear heterotrimer of $Sc@Si_{16}$–$Ti@Si_{16}$–$V@Si_{16}$ has a larger dipole moment of 15.6 D and one or more localized frontier orbitals compared to the dimer. These dimers and trimers are the smallest assembled BCSs, and the theoretical insight allows combination of

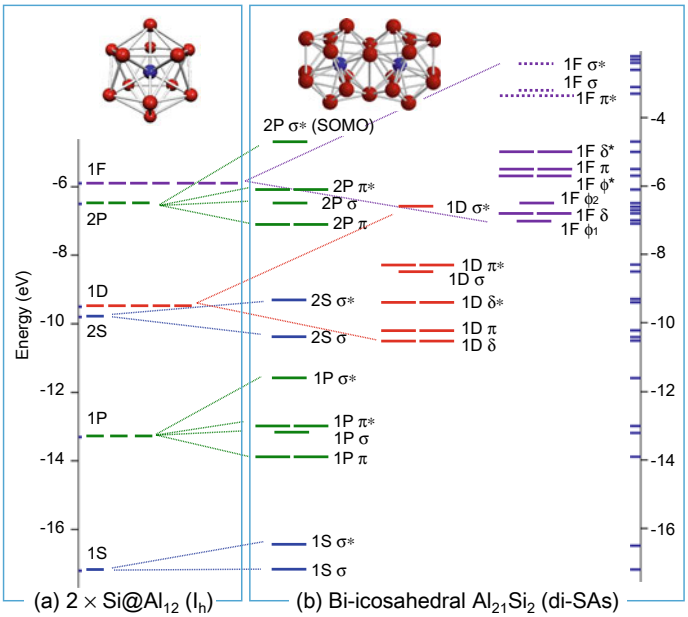

Fig. 7.20 Calculated energy diagram of **a** icosahedral Si@Al_{12} and **b** bi-icosahedral $Al_{21}Si_2$ neutral using the linear combination of SAOs (LCSAO) of the dimeric Si@Al_{12} superatom. With face sharing of Al_3, nine electrons are subtracted in the $Al_{21}Si_2$ neutral compared to two Si@Al_{12}. Solid lines show filled or half-filled states, whereas dotted lines show unoccupied states. The LCSAO-MO of 2P σ* is a SOMO for the $Al_{21}Si_2$ neutral, while the LCSAO-MO of 1F δ* is a HOMO for the $Al_{21}Si_2$ cation. Reproduced from Ref. [39] with permission from the PCCP Owner Societies

different BCSs having various central atoms to create new nanoscale materials [82, 83], which will establish a new area in the field of NC science.

7.5 Conclusions

The metal-atom-encapsulating Si_{16} cage (METS) is a novel nanostructure that was synthesized in the gas phase, and the structural properties were successfully characterized in 2017 after a long research period of over 30 years [12]. The BCS formation features synergistic generation from Si and M atomic vapor. In the highly symmetrical T_d structure, in which 16 Si atoms form a spherical outer shell, the total number of valence electrons is controlled by replacing the central metal atom. M@Si_{16} is regarded as a representative "superatoms" in which 17 atoms in total behave as a new "atom". For example, Ta@Si_{16} is a superatom with one excess electron, which is like an alkali-metal atom such as Li and Na. By replacing the central metal atom with various metal atoms, the electronic properties are designed while retaining the structural motif, and then their aggregates and hetero-interface exhibit distinct chemical and

physical properties. Furthermore, chemical ligation would modify their properties to form designer nanomaterials. The BCS nanomaterials will show novel optical and conduction properties, and $M@Si_{16}$ BCS itself exhibits new bonding features. The BCS might enable a paradigm shift in Si-based nanoscale material to overcome the integration limit of current top-down Si electronics together with $M@Ge_{16}$ BCSs [61, 84].

For Al-based BCS, $X@Al_{12}$ (X = B, Si, and P) BCSs behave as halogen-like, rare gas-like, and alkali metal-like superatoms, where small atoms are preferred as central atoms from trivalent to pentavalent atoms of main group elements. Since $Si@Al_{12}^{+/0/-}$ BCSs retain the cage structure by charge exchange from the $Si@Al_{12}$ neutral in I_h symmetry, the $Si@Al_{12}$ superatoms are stable against charge transfer, affording promising BCS assemblies for an electronic device. The theoretical analysis showed that the SAO of bi-icosahedral $Al_{21}Si_2$ can be represented by superposing two $Si@Al_{12}$ BCSs. Using the LCSAO, a MO picture for di-SAs is obtained similar to the LCAO.

Finally, the BCS assembly can apparently create new nanoscale materials; hetero-assembly of an $M@Si_{16}$ or $X@Al_{12}$ BCS comprising different central atom BCSs is theoretically predicted to show an electronic transition relevant to charge transfer. Beyond $M@Si_{16}$ and $X@Al_{12}$ BCSs themselves, these BCS assemblies will further widen a rich diversity to fabricate nanoscale functional materials, and along with that *superatom periodic table* would evolve from these BCS family members.

Acknowledgments This work is partly supported by the program of Exploratory Research for Advanced Technology (ERATO) in Japan Science and Technology Agency (JST) entitled with "Nakajima Designer Nanocluster Assembly Project", by JSPS KAKENHI of Grant-in-Aids for Scientific Research (A) no. 15H02002, and by JSPS KAKENHI of Challenging Research (Pioneering) no. 17H06226. This research is in collaboration with co-authors of Refs. [9–13], including Dr. Hironori Tsunoyama, Dr. Masahiro Shibuta, Dr. Masato Nakaya, Dr. Toyoaki Eguchi, Dr. Takeshi Iwasa, Dr. Kiichirou Koyasu, Professor Norihiro Tokitoh (Kyoto Univ.), and Associate Professor Yoshiyuki Mizuhata (Kyoto Univ.).

References

1. Moore, G.E.: Cramming more components onto integrated circuits. Electronics 114–117 (1965)
2. Canham, L.T.: Silicon quantum wire array fabrication by electrochemical and chemical dissolution of wafers. Appl. Phys. Lett. **57**, 1046–1048 (1990)
3. Walters, R.J., Bourianoff, G.I., Atwater, H.A.: Field-effect electroluminescence in silicon nanocrystals. Nat. Mater. **4**, 143–146 (2005)
4. Hochbaum, A.I., Chen, R., Delgado, R.D., Liang, W., Garnett, E.C., Najarian, M., Majumdar, A., Yang, P.: Enhanced thermoelectric performance of rough silicon nanowires. Nature **451**, 163–167 (2008)
5. Boukai, A.I., Bunimovich, Y., Tahir-Kheli, J., Yu, J.-K., Goddard III, W.A., Heath, J.R.: Silicon nanowires as efficient thermoelectric materials. Nature **451**, 168–171 (2008)
6. Kroto, H.W., Heath, J.R., O'Brien, S.C., Curl, R.F., Smalley, R.E.: C_{60}: Buckminsterfullerene. Nature **318**, 162–163 (1985)

7. Beck, S.M.: Studies of silicon cluster-metal atom compound formation in a supersonic molecular beam. J. Chem. Phys. **87**, 4233–4234 (1987)
8. Beck, S.M.: Mixed metal-silicon clusters formed by chemical reaction in a supersonic molecular beam: implications for reactions at the metal/silicon interface. J. Chem. Phys. **90**, 6306–6312 (1989)
9. Koyasu, K., Akutsu, M., Mitsui, M., Nakajima, A.: Selective formation of MSi_{16} (M = Sc, Ti, and V). J. Am. Chem. Soc. **127**, 4998–4999 (2005)
10. Nakaya, M., Iwasa, T., Tsunoyama, H., Eguchi, T., Nakajima, A.: Formation of a superatom monolayer using gas-phase-synthesized Ta@Si_{16} nanocluster ions. Nanoscale **6**, 14702–14707 (2014)
11. Shibuta, M., Ohta, T., Nakaya, M., Tsunoyama, H., Eguchi, T., Nakajima, A.: Chemical characterization of an alkali-like superatom consisting of a Ta-encapsulating Si_{16} Cage. J. Am. Chem. Soc. **137**, 14015–14018 (2015)
12. Tsunoyama, H., Akatsuka, H., Shibuta, M., Iwasa, T., Mizuhata, Y., Tokitoh, N., Nakajima, A.: Development of integrated dry-wet synthesis method for metal encapsulating silicon cage superatoms of M@Si_{16} (M = Ti and Ta). J. Phys. Chem. C **121**, 20507–20516 (2017)
13. Tsunoyama, H., Shibuta, M., Nakaya, M., Eguchi, T., Nakajima, A.: Synthesis and characterization of metal-encapsulating Si_{16} cage superatoms. Acc. Chem. Res. **51**, 1735–1745 (2018)
14. Heath, J.R., O'Brien, S.C., Zhang, Q., Liu, Y., Curl, R.F., Kroto, H.W., Tittel, F.K., Smalley, R.E.: Lanthanum complexes of spheroidal carbon shells. J. Am. Chem. Soc. **107**, 7779–7780 (1985)
15. Sanekata, M., Koya, T., Nagano, S., Negishi, Y., Nakajima, A., Kaya, K.: Electronic and geometric structures of metal-silicide clusters. Trans. Mater. Res. Soc. Jpn **25**, 1003–1006 (2000)
16. Kumar, V., Kawazoe, Y.: Metal-encapsulated fullerenelike and cubic caged clusters of silicon. Phys. Rev. Lett. **87**, 045503 (2001)
17. Hiura, H., Miyazaki, T., Kanayama, T.: Formation of metal-encapsulating Si cage clusters. Phys. Rev. Lett. **86**, 1733–1736 (2001)
18. Lu, J., Nagase, S.: Structural and electronic properties of metal-encapsulated silicon clusters in a large size range. Phys. Rev. Lett. **90**, 115506 (2003)
19. Ohara, M., Koyasu, K., Nakajima, A., Kaya, K.: Geometric and electronic structures of metal (M)-doped silicon clusters (M = Ti, Hf, Mo and W). Chem. Phys. Lett. **371**, 490–497 (2003)
20. Zheng, W., Nilles, J.M., Radisic, D., Bowen, K.H.: Photoelectron spectroscopy of chromium-doped silicon cluster anions. J. Chem. Phys. **122**, 071101 (2005)
21. Jaeger, J.B., Jaeger, T.D., Duncan, M.A.: Photodissociation of metal-silicon clusters: encapsulated versus surface-bound metal. J. Phys. Chem. A **110**, 9310–9314 (2006)
22. Reveles, J.U., Khanna, S.N.: Electronic counting rules for the stability of metal-silicon clusters. Phys. Rev. B **74**, 035435 (2006)
23. Torres, M.B., Fernández, E.M., Balbás, L.C.: Theoretical study of isoelectronic Si_nM clusters (M = Sc^-, Ti, V^+; n = 14–18). Phys. Rev. B **75**, 205425 (2007)
24. Lau, J.T., Hirsch, K., Klar, P., Langenberg, A., Lofink, F., Richter, R., Rittmann, J., Vogel, M., Zamudio-Bayer, V., Möller, T., von Issendorff, B.: X-ray spectroscopy reveals high symmetry and electronic shell structure of transition-metal-doped silicon clusters. Phys. Rev. A **79**, 053201 (2009)
25. Claes, P., Janssens, E., Ngan, V.T., Gruene, P., Lyon, J.T., Harding, D.J., Fielicke, A., Nguyen, M.T., Lievens, P.: Structural identification of caged vanadium doped silicon clusters. Phys. Rev. Lett. **107**, 173401 (2011)
26. Knight, W.D., de Heer, W.A., Clemenger, K., Saunders, W.A., Chou, M.Y., Cohen, M.L.: Electronic shell structure and abundances of sodium clusters. Phys. Rev. Lett. **52**, 2141–2143 (1984)
27. de Heer, W.A.: The physics of simple metal clusters: experimental aspects and simple models. Rev. Mod. Phys. **65**, 611–676 (1993)
28. Brack, M.: The physics of simple metal clusters: self-consistent jellium model and semiclassical approaches. Rev. Mod. Phys. **65**, 677–732 (1993)

29. Jena, P.: Beyond the periodic table of elements: the role of superatoms. J. Phys. Chem. Lett. **4**, 1432–1442 (2013)
30. Luo, Z., Castleman Jr., A.W., Khanna, S.N.: Reactivity of metal clusters. Chem. Rev. **116**, 14456–14492 (2016)
31. Tomalia, D.A., Khanna, S.N.: A systematic framework and nanoperiodic concept for unifying nanoscience: hard/soft nanoelements, superatoms, meta-atoms, new emerging properties, periodic property patterns, and predictive mendeleev-like nanoperiodic tables. Chem. Rev. **116**, 2705–2774 (2016)
32. Reber, A.C., Khanna, S.N.: Superatoms: electronic and geometric effects on reactivity. Acc. Chem. Res. **50**, 255–263 (2017)
33. Jena, P., Sun, Q.: Super atomic clusters: design rules and potential for building blocks of materials. Chem. Rev. **118**, 5755–5870 (2018)
34. Nakajima, A., Kishi, T., Sugioka, T., Kaya, K.: Electronic and geometric structures of aluminum-boron negative cluster ions ($Al_nB_m^-$). Chem. Phys. Lett. **187**, 239–244 (1991)
35. Nakajima, A., Hoshino, K., Naganuma, T., Sone, Y., Kaya, K.: Ionization potentials of aluminum-sodium bimetallic clusters (Al_nNa_m). J. Chem. Phys. **95**, 7061–7066 (1991)
36. Hoshino, K., Watanabe, K., Konishi, Y., Taguwa, T., Nakajima, A., Kaya, K.: Ionization potentials of aluminum-cesium bimetallic clusters (Al_nCs_m). Chem. Phys. Lett. **231**, 499–503 (1994)
37. Kawamata, H., Negishi, Y., Nakajima, A., Kaya, K.: Electronic properties of substituted aluminum clusters by boron and carbon atoms ($Al_nB_m^-/Al_nC_m^-$); new insights into s-p hybridization and perturbed shell structures. Chem. Phys. Lett. **337**, 255–262 (2001)
38. Akutsu, M., Koyasu, K., Atobe, J., Hosoya, N., Miyajima, K., Mitsui, M., Nakajima, A.: Experimental and theoretical characterization of aluminum-based binary superatoms of $Al_{12}X$ and their cluster salts. J. Phys. Chem. A **110**, 12073–12076 (2006)
39. Akutsu, M., Koyasu, K., Atobe, J., Miyajima, K., Mitsui, M., Tsunoyama, H., Nakajima, A.: Geometric and electronic properties of Si-atom doped Al clusters: robustness of binary superatoms against charging. Phys. Chem. Chem. Phys. **19**, 20401–20411 (2017)
40. Tsunoyama, H., Akutsu, M., Koyasu, K., Nakajima, A.: Stability for binary $Al_{12}X$ nanoclusters (X = Sc and Ti): superatom or Wade's polyhedron. J. Phys. Condensed Matter **30**, 494004 (2018)
41. Iwasa, T., Nakajima, A.: Geometric, electronic, and optical properties of a superatomic heterodimer and trimer: $Sc@Si_{16}$–$V@Si_{16}$ and $Sc@Si_{16}$–$Ti@Si_{16}$–$V@Si_{16}$. J. Phys. Chem. C **116**, 14071–14077 (2012)
42. Iwasa, T., Nakajima, A.: Geometric, electronic, and optical properties of monomer and assembly of endohedral aluminum superatomic clusters. J. Phys. Chem. C **117**, 21551–21557 (2013)
43. Iwasa, T., Nakajima, A.: Geometric, electronic, and optical properties of a boron-doped aluminum cluster of $B_2Al_{21}^-$. Chem. Phys. Lett. **582**, 100–104 (2013)
44. Koyasu, K., Atobe, J., Akutsu, M., Mitsui, M., Nakajima, A.: Electronic and geometric stabilities of clusters with transition metal encapsulated by silicon. J. Phys. Chem. A **111**, 42–49 (2007)
45. Nakajima, A.: Study on electronic properties of composite clusters toward nanoscale functional advanced materials. Bull. Chem. Soc. Jpn **86**, 414–437 (2013)
46. Even, U., Jortner, J., Noy, D., Lavie, N., Cossart-Magos, C.: Cooling of large molecules below 1 K and He clusters formation. J. Chem. Phys. **112**, 8068–8071 (2000)
47. Geohegan, D.B.: Imaging and blackbody emission spectra of particulates generated in the KrF-laser ablation of BN and $YBa_2Cu_3O_{7-x}$. Appl. Phys. Lett. **62**, 1463–1465 (1993)
48. Geusic, M.E., Morse, M.D., O'Brien, S.C., Smalley, R.E.: Surface reactions of metal clusters I: the fast flow cluster reactor. Rev. Sci. Instrum. **56**, 2123–2130 (1985)
49. Miyajima, K., Muraoka, K., Hashimoto, M., Yasuike, T., Yabushita, S., Nakajima, A., Kaya, K.: The quasi-band electronic structure of $V_n(Benzene)_{n+1}$ clusters. J. Phys. Chem. A **106**, 10777–10781 (2002)
50. Cheshnovsky, O., Yang, S.H., Pettiette, C.L., Craycraft, M.J., Smalley, R.E.: Magnetic time-of-flight photoelectron spectrometer for mass-selected negative cluster ions. Rev. Sci. Instrum. **58**, 2131–2137 (1987)

51. Ganteför, G., Meiwes-Broer, K.H., Lutz, H.O.: Photodetachment spectroscopy of cold aluminum cluster anions. Phys. Rev. A **37**, 2716–2718 (1988)
52. Ganteför, G., Gausa, M., Meiwes-Broer, K.H., Lutz, H.O.: Ultraviolet photodetachment spectroscopy on jet-cooled metal-cluster anions. Faraday Discuss. Chem. Soc. **86**, 197–208 (1988)
53. Nakajima, A., Taguwa, T., Hoshino, K., Sugioka, T., Naganuma, T., Ono, F., Watanabe, K., Nakao, K., Konishi, Y., Kishi, R., Kaya, K.: Photoelectron spectroscopy of $(C_6F_6)_n^-$ and $(Au\text{-}C_6F_6)^-$ clusters. Chem. Phys. Lett. **214**, 22–26 (1993)
54. Ho, J., Ervin, K.M., Lineberger, W.C.: Photoelectron spectroscopy of metal cluster anions: Cu_n^-, Ag_n^-, and Au_n^-. J. Chem. Phys. **93**, 6987–7002 (1990)
55. Moore, C.E.: Atomic energy levels as derived from the analyses of optical spectra. NSRDS-NBS, 35, vol. 3. U.S. National Bureau of Standards: Washington, DC (1971)
56. Koyasu, K., Atobe, J., Furuse, S., Nakajima, A.: Anion photoelectron spectroscopy of transition metal- and lanthanide metal-silicon clusters: MSi_n^- ($n = 6$–20). J. Chem. Phys. **129**, 214301 (2008)
57. Kawamata, H., Negishi, Y., Kishi, R., Iwata, S., Nakajima, A., Kaya, K.: Photoelectron spectroscopy of silicon-fluorine binary cluster anions ($Si_nF_m^-$). J. Chem. Phys. **105**, 5369–5376 (1996)
58. Negishi, Y., Kawamata, H., Hayase, T., Gomei, M., Kishi, R., Hayakawa, F., Nakajima, A., Kaya, K.: Photoelectron spectroscopy of germanium-fluorine binary cluster anions: the HOMO-LUMO gap estimation of gen clusters. Chem. Phys. Lett. **269**, 199–207 (1997)
59. Kishi, R., Negishi, Y., Kawamata, H., Iwata, S., Nakajima, A., Kaya, K.: Geometric and electronic structures of fluorine bound silicon clusters. J. Chem. Phys. **108**, 8039–8058 (1998)
60. Wang, X.B., Ding, C.F., Wang, L.S.: High resolution photoelectron spectroscopy of C_{60}^-. J. Chem. Phys. **110**, 8217–8220 (1999)
61. Furuse, S., Koyasu, K., Atobe, J., Nakajima, A.: Experimental and theoretical characterization of MSi_{16}^-, MGe_{16}^-, MSn_{16}^-, and MPb_{16}^- (M = Ti, Zr, and Hf): the role of cage aromaticity. J. Chem. Phys. **129**, 064311 (2008)
62. Bromann, K., Felix, C., Brune, H., Harbich, W., Monot, R., Buttet, J., Kern, K.: Controlled deposition of size-selected silver nanoclusters. Science **274**, 956–958 (1996)
63. Haberland, H., Karrais, M., Mall, M.: A new type of cluster and cluster ion source. Z. Phys. D **20**, 413–415 (1991)
64. Haberland, H., Karrais, M., Mall, M., Thurner, Y.: Thin films from energetic cluster impact: a feasibility study. J. Vac. Sci. Technol., A **10**, 3266–3271 (1992)
65. Tsunoyama, H., Zhang, C., Akatsuka, H., Sekiya, H., Nagase, T., Nakajima, A.: Development of high-flux ion source for size-selected nanocluster ions based on high-power impulse magnetron sputtering. Chem. Lett. **42**, 857–859 (2013)
66. Zhang, C., Tsunoyama, H., Akatsuka, H., Sekiya, H., Nagase, T., Nakajima, A.: Advanced nanocluster ion source based on high-power impulse magnetron sputtering and time-resolved measurements of nanocluster formation. J. Phys. Chem. A **117**, 10211–10217 (2013)
67. Zhang, C., Tsunoyama, H., Feng, Y., Nakajima, A.: Extended Smoluchowski model for the formation of size-selected silver nanoclusters generated via modulated pulsed power magnetron sputtering. J. Phys. Chem. C **120**, 5667–5672 (2016)
68. Nakaya, M., Iwasa, T., Tsunoyama, H., Eguchi, T., Nakajima, A.: Heterodimerization via the covalent bonding of $Ta@Si_{16}$ nanoclusters and C_{60} molecules. J. Phys. Chem. C **119**, 10962–10968 (2015)
69. Ohta, T., Shibuta, M., Tsunoyama, H., Eguchi, T., Nakajima, A.: Charge transfer complexation of Ta-encapsulating $Ta@Si_{16}$ superatom with C_{60}. J. Phys. Chem. C **120**, 15265–15271 (2016)
70. Shibuta, M., Kamoshida, T., Ohta, T., Tsunoyama, H., Nakajima, A.: Alkali-like superatom chemistry of group-5 metal encapsulating Si_{16} cage; $M@Si_{16}$ (M = V, Nb, Ta). Comm. Chem. **1**, 50 (2018)
71. Gomoyunova, M.V., Pronin, I.I., Malygin, D.E., Gall, N.R., Vyalikh, D.V., Molodtsov, S.L.: Photoemission study of cobalt interaction with the oxidized Si(100) 2×1 surface. Surf. Sci. **600**, 2449–2456 (2006)

72. van der Veen, J.F., Himpsel, F.J., Eastman, D.E.: Chemisorption-induced 4f-core-electron binding-energy shifts for surface atoms of W(111), W(100), and Ta(111). Phys. Rev. B **25**, 7388–7397 (1982)
73. Even, U., Dick, B.: Computer optimization for high-resolution time-of-flight mass spectrometer. Rev. Sci. Instrum. **71**, 4415–4420 (2000)
74. Li, X., Wu, H., Wang, X.B., Wang, L.S.: *s-p* hybridization and electron shell structures in aluminum clusters: a photoelectron spectroscopy study. Phys. Rev. Lett. **81**, 1909–1912 (1998)
75. Koyasu, K., Akutsu, M., Atobe, J., Mitsui, M., Nakajima, A.: Electronic properties of Cs-atom doped aluminum and silicon clusters: Al_nCs_m and Si_nCs_m. Chem. Phys. Lett. **421**, 534–539 (2006)
76. Shriver, D. F.; Atkins, P. W., *Inorganic Chemistry*. **1999**, Oxford Univ. Press, 3rd edn
77. Mackay, A.L.: A dense non-crystallographic packing of equal spheres. Acta Crystallogr. **15**, 916–918 (1962)
78. Kishi, R., Iwata, S., Nakajima, A., Kaya, K.: Geometric and electronic structures of silicon—sodium binary clusters. I. Ionization energy of Si_nNa_m. J. Chem. Phys. **107**, 3056–3070 (1997)
79. Gong, X.G., Kumar, V.: Enhanced stability of magic clusters: a case study of icosahedral $Al_{12}X$, X = B, Al, Ga, C, Si, Ge, Ti, As. Phys. Rev. Lett. **70**, 2078–2081 (1993)
80. Li, X., Wang, L.-S.: Experimental search and characterization of icosahedral clusters: $Al_{12}X^-$ (X = C, Ge, Sn, Pb). Phys. Rev. B **65**, 153404 (2002)
81. Lu, Q.L., Jalbout, A.F., Luo, Q.Q., Wan, J.G., Wang, G.H.: Theoretical study of hydrogenated Mg, Ca@Al_{12} Clusters. J. Chem. Phys. **128**, 224707 (2008)
82. Khanna, S.N., Jena, P.: Assembling Crystals from Clusters. Phys. Rev. Lett. **69**, 1664–1667 (1992)
83. Claridge, S.A., Castleman Jr., A.W., Khanna, S.N., Murray, C.B., Sen, A., Weiss, P.S.: Cluster-assembled materials. ACS Nano **3**, 244–255 (2009)
84. Atobe, J., Koyasu, K., Furuse, S., Nakajima, A.: Anion photoelectron spectroscopy of germanium and tin clusters containing a transition- or lanthanide-metal atom; MGen^- (n = 8–20) and MSnn^- (n = 15–17) (M = Sc–V, Y–Nb, and Lu–Ta). Phys. Chem. Chem. Phys. **14**, 9403–9410 (2012)